Mon. Not. R. Astron. Soc. **373,** 411–424 (2006) doi:10.1111/j.1365-2966.2006.11047.x

Class I methanol masers in the outflow of IRAS 16 547–4247

M. A. Voronkov,[1,2★] K. J. Brooks,[1] A. M. Sobolev,[3] S. P. Ellingsen,[4] A. B. Ostrovskii[3] and J. L. Caswell[1]

[1]*Australia Telescope National Facility CSIRO, PO Box 76, Epping, NSW 1710, Australia*
[2]*Astro Space Centre, Profsouznaya st. 84/32, 117997 Moscow, Russia*
[3]*Ural State University, Lenin ave. 51, 620083 Ekaterinburg, Russia*
[4]*School of Mathematics and Physics, University of Tasmania, GPO Box 252-37, Hobart, Tasmania 7000, Australia*

Accepted 2006 September 7. Received 2006 September 7; in original form 2006 June 23

ABSTRACT

The Australia Telescope Compact Array (ATCA) has been used to image class I methanol masers at 9.9, 25 (a series from $J = 2$ to 9), 84, 95 and 104 GHz located in the vicinity of IRAS 16 547−4247 (G343.12−0.06), a luminous young stellar object known to harbour a radio jet. The detected maser emission consists of a cluster of six spots spread over an area of 30 arcsec. Five spots were detected in only the 84- and 95-GHz transitions (for two spots the 84-GHz detection is marginal), while the sixth spot shows activity in all 12 observed transitions. We report the first interferometric observations of the rare 9.9- and 104-GHz masers. It is shown that the spectra contain a very narrow spike ($< 0.03\,\mathrm{km\,s^{-1}}$) and the brightness temperature in these two transitions exceeds 5.3×10^7 and 2.0×10^4 K, respectively. The three most southern maser spots show a clear association with the shocked gas traced by the H_2 2.12-μm emission associated with the radio jet and their velocities are close to that of the molecular core within which the jet is embedded. This fact supports the idea that the class I masers reside in the interface regions of outflows. Comparison with OH masers and infrared data reveals a potential discrepancy in the expected evolutionary state. The presence of the OH masers usually means that the source is evolved, but the infrared data suggest otherwise. The lack of any class II methanol maser emission at 6.7 GHz in the source raises an additional question, Is this source too young or too old to have a 6.7-GHz maser? We argue that both cases are possible and suggest that the evolutionary stage where the class I masers are active, may last longer and start earlier than when the class II masers are active. However, it is currently not possible to reveal the exact evolutionary status of IRAS 16 547−4247.

Key words: masers – ISM: jets and outflows – ISM: molecules.

1 INTRODUCTION

Methanol masers are commonly found in massive star-forming regions. They fall into two categories first defined by Batrla & Menten (1988) and further considered by Voronkov et al. (2005b): class II masers (of which the 6.7 GHz is the best known and usually strongest) are closely associated with infrared sources and reside in the close environment of exciting (proto-)stars. In contrast, class I masers (e.g. 95 GHz) are usually found offset (by up to a parsec) from continuum sources (e.g. Kurtz, Hofner & Álvarez 2004). Theoretical calculations strongly suggest that class I masers are pumped via collisions with the molecular hydrogen in contrast to class II masers, which have a radiative pump (e.g. Cragg et al. 1992; Voronkov 1999; Voronkov et al. 2005b).

Class I masers are relatively poorly studied. There is direct observational evidence to suggest a relationship between these masers and outflows in a number of sources (Plambeck & Menten 1990; Menten 1996), although another scenario, which involves cloud–cloud collisions, has also been proposed (Sobolev 1992; Mehringer & Menten 1996; Salii, Sobolev & Kalinina 2002). The common point of these two scenarios is the presence of shocks. There is observational evidence that methanol abundance is significantly increased in the shock processed regions (e.g. Gibb & Davis 1998) and the gas is expected to be heated and compressed in such regions providing more frequent collisions and, therefore, more efficient pumping.

To further investigate the relationship of different class I maser transitions with outflows and to provide data for theoretical studies, we have made interferometric observations of 12 class I maser transitions towards IRAS 16 547−4247 (G343.12−0.06) using the Australia Telescope Compact Array (ATCA). This is a significant

★E-mail: maxim.voronkov@csiro.au

fraction (50 per cent according to Müller, Menten & Mäder 2004) of all known class I maser transitions, the majority of which belong to the $J_2 - J_1$ E series. We observed at least one transition from each transition series known to exhibit class I maser activity (Voronkov 1999) and covered all known class I maser transitions within the frequency range of existing ATCA receivers. Only the $J = 5$ transition from the $J_2 - J_1$ E series at 25 GHz has been previously observed towards IRAS 16 547−4247 (Voronkov et al. 2005a), although with no position measurement. In this paper we present the first detection of seven other transitions from this series as well as the first detection of the 84-GHz maser towards this source. The other three transitions were detected in a number of single dish and ATCA maser line surveys (Slysh et al. 1994; Val'tts et al. 2000; Voronkov et al., unpublished observations). It is worth mentioning that this source is the only example where all these class I maser transitions have been detected together, including the relatively rare 9.9- and 104-GHz masers.

IRAS 16 547−4257 has recently been the focus of attention as the most luminous young stellar object (YSO) known to harbour a radio jet. At a distance of 2.9 kpc (Bronfman, private communication), the YSO has a bolometric luminosity of $6.2 \times 10^4\,L_\odot$, equivalent to that of a single O8 zero-age main-sequence (ZAMS) star. The jet was first detected by Garay et al. (2003) using the ATCA at 1.4, 2.5, 4.8 and 8.6 GHz and subsequently observed using the Very Large Array (VLA) at 8.5 and 14.9 GHz (Rodríguez et al. 2005). This is the first reported case of a radio jet associated with a young O-type star. Located at the centre of a massive dense molecular core (approximately $10^3\,M_\odot$), the jet is driving a highly energetic collimated bipolar outflow that extends over 1.5 pc (Brooks et al. 2003; Garay et al. 2006).

2 OBSERVATIONS

Observations were made using the ATCA in 2005 May–August with assorted array configurations and various correlator modes. The details, including the spectral resolutions, velocity coverages, full width at half-maximum (FWHM) of the primary beam and synthesized beam parameters, are summarized in Table 1. We adopted the rest frequencies determined by Müller et al. (2004). The measurement uncertainties are given in Table 1 in parentheses after each corresponding frequency. They are expressed in units of the least significant figure. Corresponding uncertainties in the radial velocity are given in the next column.

The $J = 2$, 3 and 4 transitions of the $J_2 - J_1$ E series near 25 GHz were observed in a single 8-MHz band centred on the average frequency of these transitions. The remaining transitions were observed using a separate frequency set-up for each individual transition. The correlator set-up used for observations of the $J = 5$ and 6 transitions on May 2 allowed us to observe the 24 896-MHz continuum emission with a 128-MHz bandwidth simultaneously with the spectral line observations. However, for the subsequent observations we chose a higher spectral resolution rather than a continuum channel. With the exception of the 9.9-GHz observations on June 16 two orthogonal linear polarizations were recorded. For June 16 only one linear polarization was recorded in order to obtain a larger number of spectral channels and achieve a spectral resolution comparable with that of the higher frequency transitions. It is worth noting that Wiesemeyer, Thum & Walmsley (2004) found a number of mm-wavelength class I methanol maser transitions to be polarized. The correlator set-up used in our study did not allow us to determine polarization properties. However, during the data reduction both polarizations, if present, were averaged together. Hence, all the flux densities with the exception of that at 9.9 GHz measured on June 16 are not affected by polarization. For the latter we examined the flux density measured from 10 individual scans taken at various hour angles assuming that the source was unresolved and located at the position found by the imaging. No parallactic angle dependence was found beyond the noise level of 0.3 Jy (1σ). This fact as well as a comparison with the May observations (see Section 3.3) performed in the dual polarization mode leads us to conclude that polarization effects, if present, are less than the calibration uncertainty.

The position of the phase and pointing centre was $\alpha_{2000} = 16^{\rm h}58^{\rm m}16\overset{\rm s}{.}57$, $\delta_{2000} = -42^\circ52'24\overset{''}{.}0$ in all observing sessions. Reference pointing using the source 1646−50 (which served also as a phase calibrator) was used for all observations except those at 9.9 GHz, where a global pointing model was used. From the statistics of the pointing solution the reference pointing accuracy was estimated to be 2.3 ± 0.8 arcsec for all observing runs. The accuracy of the global model (which affects the 9.9-GHz data only) was estimated to be 6 ± 3 and 10 ± 4 arcsec for the May 2 and June 16 runs, respectively. The accuracy of the reference pointing affects the accuracy of flux density measurements, particularly for sources offset

Table 1. Dates of observations, array configurations and observed transitions.

UT date	Array configuration	Transition	Frequency (MHz)	Velocity uncertainty (km s^{-1})	Primary beam (arcmin)	Synthesized beam FWHM (arcsec)	Synthesized beam pa (°)	Spectral resolution (km s^{-1})	Velocity coverage (km s^{-1})
2005 May 2	750A	9_{-1}–8_{-2} E	9936.202 (4)	0.12	5.09	No imaging		0.12	−92, +28
		2_2–2_1 E	24934.382 (5)	0.06	2.03	2.0×1.3	88	0.047	−36, +41
		3_2–3_1 E	24928.707 (7)	0.08	2.03	1.2×0.8	6	0.047	−104, −27.5
		4_2–4_1 E	24933.468 (2)	0.02	2.03	1.2×0.8	14	0.047	−46, +30
		5_2–5_1 E	24959.0789 (4)	0.005	2.03	1.2×0.7	22	0.047	−55, −18
		6_2–6_1 E	25018.1225 (4)	0.005	2.02	1.6×0.8	20	0.047	−54, −18
2005 June 16	6B	9_{-1}–8_{-2} E	9936.202 (4)	0.12	5.09	1.6×1.2	−1	0.029	−70, +26
		6_2–6_1 E	25018.1225 (4)	0.005	2.02	0.6×0.5	−5	0.023	−51, −13
		7_2–7_1 E	25124.8719 (4)	0.005	2.01	0.7×0.5	−3	0.023	−54, −16
		8_2–8_1 E	25294.4165 (4)	0.005	2.00	0.7×0.5	−3	0.023	−47, −10
		9_2–9_1 E	25541.3979 (4)	0.005	1.98	0.7×0.5	−4	0.023	−47, −10
2005 August 18	H214C	6_2–6_1 E	25018.1225 (4)	0.005	2.02	No imaging		0.023	−55, −8
		5_{-1}–4_0 E	84521.169 (10)	0.04	0.60	2.7×1.9	88	0.028	−41, −19
		8_0–7_1 A$^+$	95169.463 (10)	0.03	0.53	2.3×1.7	87	0.025	−41, −22
		11_{-1}–10_{-2} E	104300.414 (7)	0.02	0.49	2.1×1.5	88	0.022	−39, −22

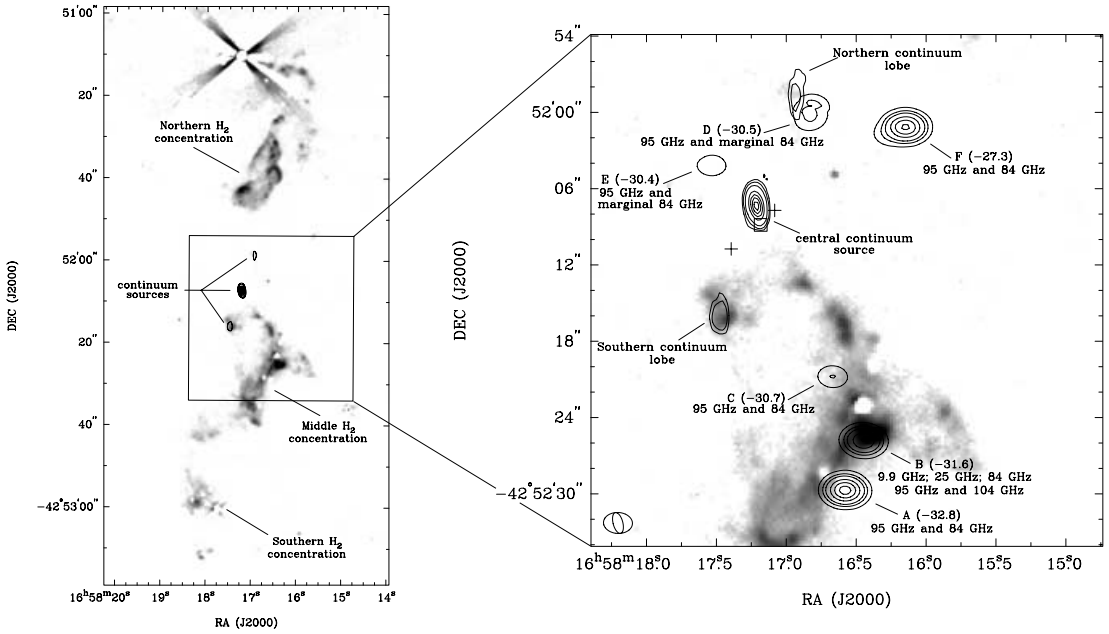

Figure 1. The general morphology of the region: the 95-GHz maser spots and the 25-GHz continuum sources are overlaid on the H_2 2.12-μm image (Brooks et al. 2003). The continuum sources are also shown on the large-scale image and believed to delineate the direction of the jet. An artefact in the northern part of the large-scale H_2 image is caused by a star. Contours in the small-scale image are (1, 2, 3, 4, 5, 7, 9) $\times 3.6\,\mathrm{Jy\,beam^{-1}}$ and (0.3, 0.5, 1, 3, 5, 7, 9) $\times 1.5\,\mathrm{mJy\,beam^{-1}}$ for the 95-GHz maser and 25-GHz continuum sources, respectively. The lowest contour of the 25-GHz continuum emission corresponds to 7σ. The noise level of the 95-GHz image varies significantly across the image (see Table 3). For spot F the lowest contour corresponds to 9σ. The numbers in parentheses are approximate peak radial velocities in $\mathrm{km\,s^{-1}}$ for each maser spot. The synthesized beam is shown in the bottom left-hand corner of the inset (small and large ellipses for 25 and 95 GHz, respectively). The open box and two crosses near the central continuum source mark the positions of the mainline OH masers and two well separated clusters of the H_2O masers, respectively.

from the pointing centre. The positional accuracy of the maser locations is primarily influenced by the quality of the phase calibration and is believed to be better than 0.5 arcsec. All 3-mm observations were undertaken as two-point mosaics. An additional pointing was offset half of the primary beam width (see Table 1) to the east from the position given above.

Data reduction was performed using the MIRIAD package (2005 August 28 release) following standard procedures with the exception of bandpass calibration. Using the UVLIN task of MIRIAD a low-order polynomial fit to the spectrum of the bandpass calibrator (1921−293) has been performed before attempting a bandpass solution with the MFCAL task. This approach enables us to achieve a higher spectral line dynamic range (i.e. detect a weaker spectral line in front of the continuum of a given flux density), although none of the data sets described in the paper turned out to be dynamic range limited.

The flux density scale at 9.9 and 25 GHz was established using the standard ATCA primary calibrator, 1934−638. For higher frequencies planetary calibration was done using Uranus. In order to assess the variability of the source some transitions were observed more than once. Two such repeated observations (see Table 1) were quite short and no imaging was possible. However, an accurate check of the flux density scale is still possible provided the source position is the same for all epochs. The accuracy of the absolute scale of flux density is estimated to be 3 and 10 per cent at 9.9 and 25 GHz, respectively.[1] The uncertainty of high-frequency planetary calibration of the ATCA has yet to be fully investigated and may be as large as 50 per cent. However, based on our experience we believe it to be better than 30 per cent for the calibration and data reduction procedure we followed in our observations. This figure is in agreement with the measured relative flux densities of the secondary calibrator at different frequencies. An additional 8 per cent flux density uncertainty related to the pointing accuracy given above exists for the high-frequency (84 and 95 GHz) features situated near the edge of the imaged field of view.

[1] For details on the calibration using 1934–638 query this calibrator at the ATCA calibrators web page (http://www.narrabri.atnf.csiro.au/calibrators).

3 RESULTS

3.1 General morphology

Fig. 1 shows an H_2 2.12-μm image of IRAS 16 47−4247 (Brooks et al. 2003). The image contains a complex chain of emission with three major concentrations consistent with the morphological characteristics of Herbig–Haro (HH) objects arising from the interaction of a collimated flow with the ambient medium (Reipurth & Bally 2001). There are a number of mechanisms responsible for excitation of 2.12-μm emission, the most common of which are fluorescence and collisional excitation in shocks (e.g. Habart et al. 2005). Several mechanisms can simultaneously contribute to the observed emission. In general, a detailed spectroscopic analysis is required to determine the exact excitation condition (e.g. Eislöffel et al. 1996; Walsh, Lee & Burton 2002). However, the morphology of the region, which suggests an interaction between the outflow and the ambient medium, together with the lack of Brγ emission which indicates that the number of ultraviolet photons is insufficient to pump the fluorescence (Brooks et al. 2003), supports the idea that most of the H_2 emission in this source traces shocked gas.

The outer concentrations of H_2 are located approximately symmetrically offset from the brightest source of the cm-wavelength radio continuum emission (see Fig. 1). This continuum source was first detected by Garay et al. (2003) and interpreted as thermal (free–free) emission from a radio jet. Garay et al. (2003) also detected two satellite continuum sources and interpreted them as the internal working surfaces of the jet. Sensitive high spatial resolution observations carried out by Rodríguez et al. (2005) resolved the northern lobe into a chain of spots aligned along the jet direction and showed that the peak spot most likely corresponds to optically thin thermal emission. The southern lobe was also resolved by Rodríguez et al. (2005), but in contrast to the northern lobe a non-thermal origin of the brightest component has been confirmed. Both thermal and non-thermal emission mechanisms are expected according to theoretical studies of electron acceleration in shock waves (e.g. Henriksen, Ptuskin & Mirabel 1991).

In addition to these sources, Rodríguez et al. (2005) detected three continuum sources displaced by a few arcseconds from the jet axis, which is thought to be a line joining the outer continuum lobes (Fig. 1). The brightest two of these sources are located between the southern non-thermal lobe and the central source and form a wiggly structure, convex in the opposite direction from the bow-shaped middle H_2 concentration. Rodríguez et al. (2005) proposed that one of these continuum sources (the most distant from the jet axis) could be associated with a young, low-mass star with a gyrosynchrotron emission. If this interpretation is correct, the curved shape of the middle H_2 concentration could be the result of an additional outflow from this less massive star. However, it follows from the large-scale distribution of the H_2 emission shown in Fig. 1 that the molecular outflow covers a rather wide area along the jet. Therefore, this morphology could also be caused by a number of factors such as irregularities in the ambient medium or precession of the jet (Brooks et al. 2003).

The expanded scale inset of Fig. 1 shows the location of all detected maser spots at 95 GHz (labelled A to F). The 25-GHz continuum emission also shown in the figure closely resembles the triple-source morphology found at lower frequencies by Garay et al. (2003). This continuum measurement and the spectral energy distribution (SED) of the source are discussed in a separate paper (Brooks et al. 2006). The outermost lobes of the H_2 emission are outside the ATCA field of view at 3 mm. The southern maser spots (labelled A to C) show a remarkable correlation with the prominent H_2 feature (Fig. 1). Contrary to our expectations based on the single-dish spectra of Val'tts et al. (2000) obtained at five offset pointings, no maser spots offset in the east–west direction were detected. Instead, a group of spots (E, D and F) was found near the edge of the field of view in the northern direction. Most likely this discrepancy is related to the pointing model used at the Mopra radio telescope during the observations of Val'tts et al.

3.2 Methanol masers

For each spot and observed frequency we produced spectra by summing the flux density in each plane of the deconvolved cube after the primary beam correction or linear mosaicing. The summation was over a box centred on the peak pixel in the image. The size of this box was chosen individually for each spot to suppress all unrelated emission (which is difficult at the edge of the field of view), and was typically about 4 arcsec. The spectra for all spots other than spot B are shown in Fig. 2. The horizontal error bars on these plots show the 3σ velocity uncertainty related to the uncertainty of the rest frequency. With the exception of spot B, all were detected only at 84 and 95 GHz, although the 84-GHz detections for spots D and E are marginal (both at the level of 4σ).

The profiles look similar at both frequencies for spot A. However, the two spectral features of spot C show significantly different 95-GHz peak flux densities, while at 84 GHz they are similar. The 84-GHz profile of spot D looks somewhat similar to its 95-GHz counterpart, giving us confidence that this marginal detection is real. The case for spot E is more doubtful, a narrow spike near $-30.33\,\mathrm{km\,s^{-1}}$ at 84 GHz may be real given the presence of a feature with a similar appearance at 95 GHz. The 84-GHz spectrum also shows a hint of broad-line emission centred at $-30.2\,\mathrm{km\,s^{-1}}$, with a narrow line at $-32.18\,\mathrm{km\,s^{-1}}$ which does not have a 95-GHz counterpart. We have formed similar spectra for adjacent areas in the image to check that these 84-GHz features are present towards the spots D and E only. However, we cannot completely exclude the possibility that they are spurious because spots D and E are located near the edge of the mosaic, and the source contains emission at different locations with overlapping velocity ranges. In the image cube these features cannot be distinguished from the edge noise. Therefore, we have not drawn any conclusions from the possible presence of 84-GHz emission towards spots D and E. The 95-GHz spectrum of spot E contains several components well spread in velocity, although the image of the spot E is simple (see Fig. 1). This is not observed for any of the other spots in this source. The presence of multiple components for spot F is more pronounced at 84 GHz. The 95-GHz profile of this spot looks like a single asymmetric broad feature. This may indicate fine scale structure, which differs at these two frequencies (i.e. there may be one more 95-GHz component).

The remaining spot B is exceptional in the sense that all observed transitions have been detected towards it. Corresponding spectra are shown in Fig. 3. As in Fig. 2, the error bars show the 3σ velocity uncertainty, with the exception of the high J 25-GHz transitions where the uncertainty is less than the spectral resolution, and therefore is not shown. The 95-GHz profile is wider than the 84-GHz one and has an additional emission component. In contrast, all 25-GHz profiles are narrow. The 9.9- and 104-GHz profiles resemble each other and have an almost single spectral channel spike on top of a broad symmetric line.

To provide quantitative characteristics of the observed spectral profiles each of them has been fitted with a number of Gaussian components. The results of these fits are summarized in Table 2. As before, the uncertainties are given in parentheses and expressed in units of the least significant figure. The first column represents the name of the spot. The next six columns are self-explanatory and contain the parameters of each Gaussian component. The spectral and spatial domain were fitted separately. First, the peak radial velocity with respect to the local standard of rest (LSR), the line widths (FWHM) and the peak flux densities listed in the columns 2, 5 and 6 were determined directly from the spectra shown in Figs 2 and 3. Then a two-dimensional (2D) Gaussian source was fitted to the image of a single plane of the spectral cube, which corresponded to the peak velocity of each Gaussian component. This second fit gave the position and the deconvolved source size estimate shown in columns 3, 4 and 7. The latter is obtained under the assumption that the synthesized beam is known exactly and the source is circular. In the size column of Table 2, two components are described as 'unresolved' (the fitted size in these cases was slightly smaller than the beam, owing to the effect of noise). Marginal 84-GHz detections towards the spots D and E are hidden in the edge noise in the image. Therefore, no second stage fit has been done for them. However, the position of these 84-GHz features, if they are real, is within 4 arcsec (the box size used in forming the spectra from

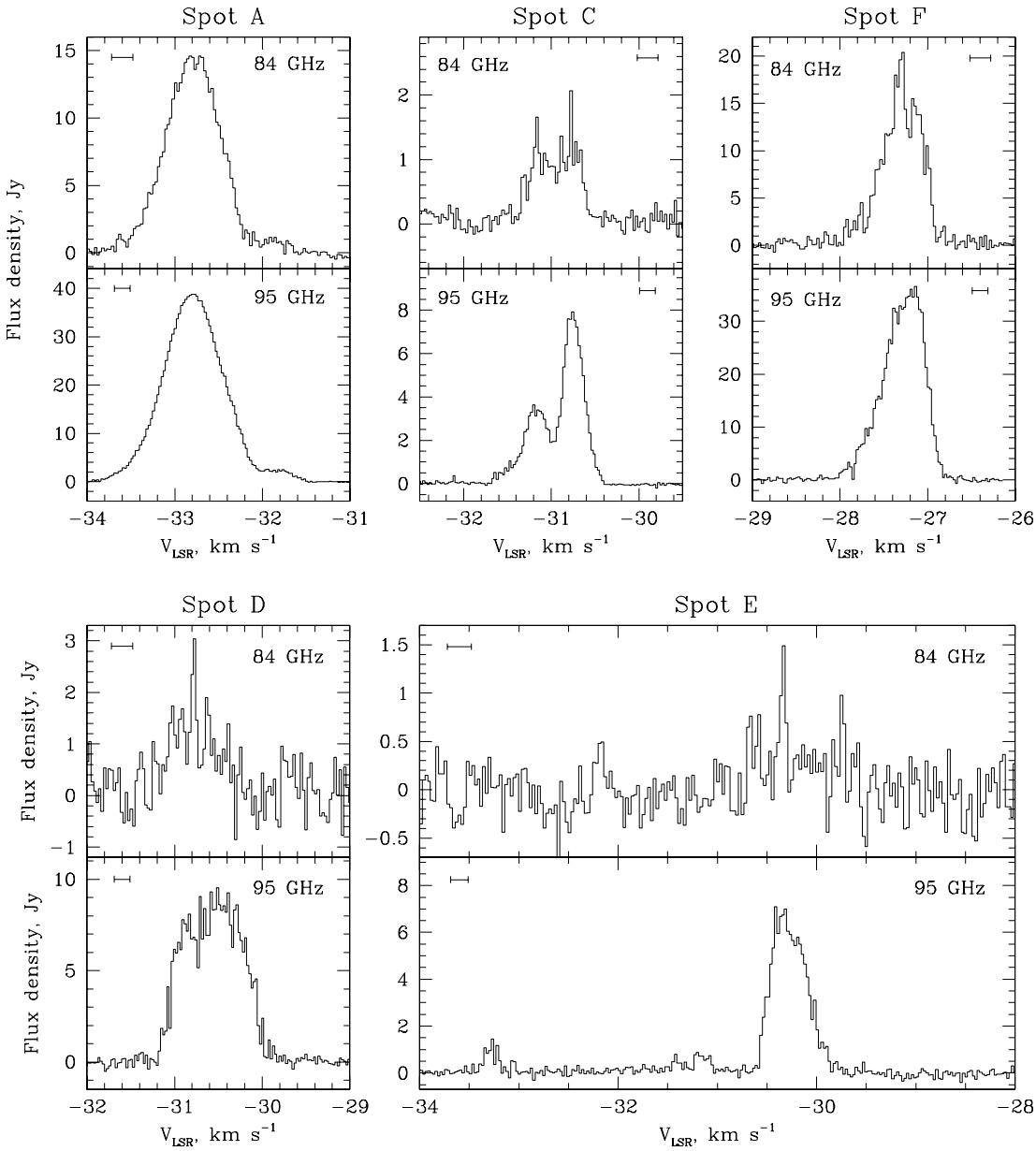

Figure 2. Spectra of spots A, C–F at 84 GHz (upper plots) and 95 GHz (lower plots). Spots D and E were marginal detections at 84 GHz. The error bar near the top of each plot shows the 3σ velocity uncertainty corresponding to the uncertainty in rest frequency (see Table 1).

the image cube) of the position of the appropriate 95-GHz spot. A combination of a δ function and a Gaussian was used to fit the 9.9- and 104-GHz spectra, which contain a narrow spike. An upper limit equal to the spectral resolution is given in the line width column of Table 2 for such narrow spikes. The flux density of these spikes exceeds the rms noise eight and 22 times for the 9.9- and 104-GHz profiles, respectively (see Table 2). This fact leaves no doubts that the spikes are real.

All uncertainties listed in columns 3–7 are the formal uncertainties of the Gaussian fit (1σ). The formal uncertainty of the peak velocity is always half of that for the line width. However, due to blending of different components seen in most cases, there are likely to be systematic errors. Because of these errors, the individual components are likely to appear closer to each other according to the fit (given in Table 2) than they are in reality, both in the spatial domain and velocity. Their linewidths and sizes are likely to be overestimated. In some cases, a superposition of two components is completely dominated by the brightest feature located at approximately the same velocity as the weaker one. We were unable to produce a reliable image plane fit for a weaker line in such situations.

The rest of the columns describe each line profile as a whole, providing more robust values than the results of the Gaussian fit. The columns are the peak LSR velocity and the corresponding flux density, the area under the line profile (the integrated flux density) and the brightness temperature lower limit. The latter is calculated using the peak (in the spectral domain) of the total brightness contained in the same region of image, which was used to compute the spectra. This approach is more appropriate for unresolved or barely resolved sources and does not depend on (sometimes very crude) size estimates. Such high values of the brightness temperature (lower limits from 6×10^3 to 5×10^7 K, see Table 2) are generally considered as an indication that the detections have a maser rather than thermal

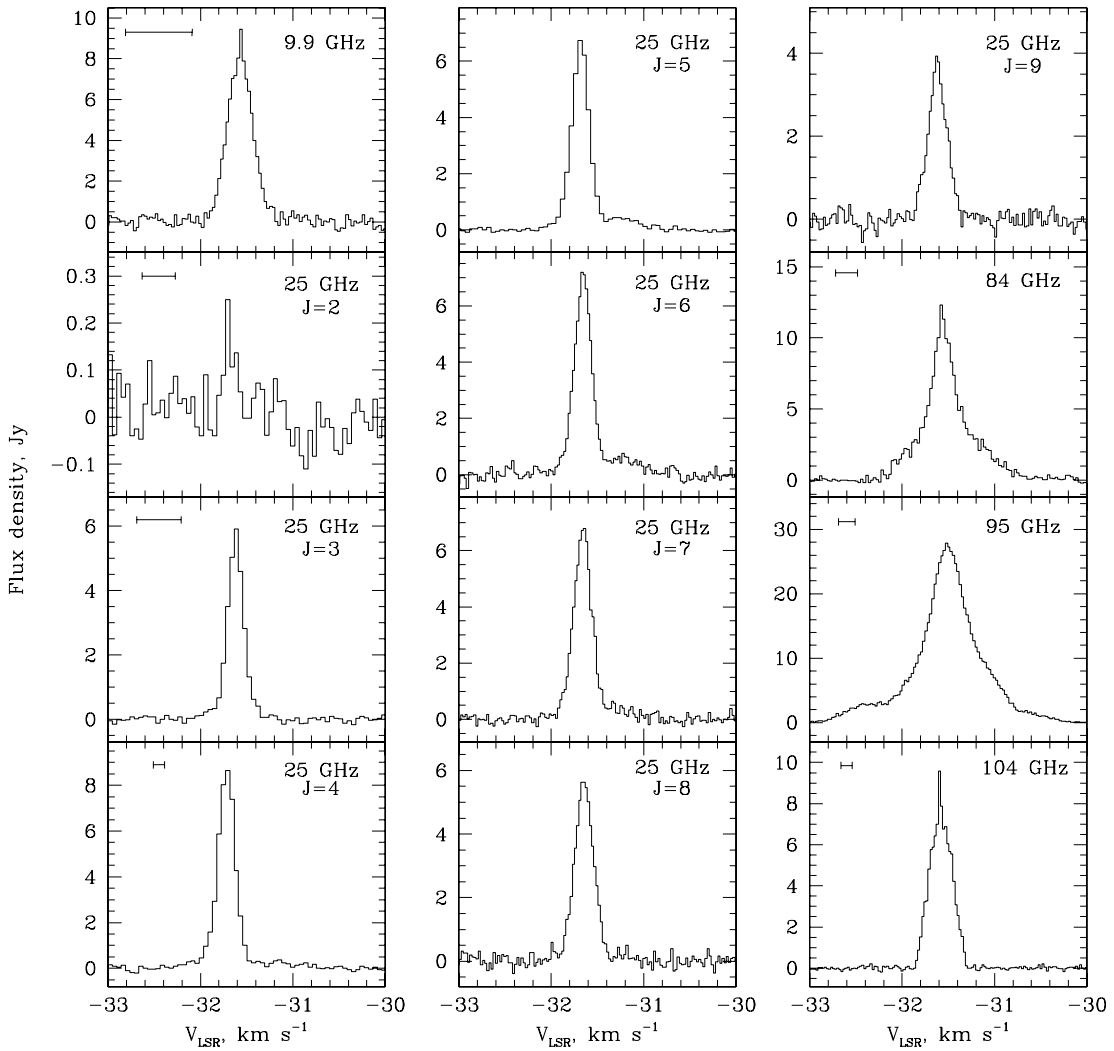

Figure 3. Spectra of spot B, where masers in all observed transitions were detected. The error bar at the top of some plots shows the 3σ velocity uncertainty corresponding to the uncertainty in rest frequency (see Table 1). For $J = 5$–9 transitions at 25 GHz this uncertainty is below the spectral resolution and, therefore, is not shown.

origin. The uncertainty of the peak velocity is equal to the spectral resolution, which is different in each particular case (see Table 1). A systematic offset of the velocity scale for a transition can be caused by rest frequency uncertainties, which are also listed in Table 1. This also applies to the peak velocity of the Gaussian components. The uncertainty of the integrated flux density was obtained from either the noise level in the spectrum (see below) or the offset from zero of the mean flux density in the line-free part of the spectrum; we have quoted the larger of these two uncertainties in each case.

To quantify the noise and provide useful upper limits for transitions which have not been detected, we have calculated the rms noise in the spectra constructed for each spot. The spectra for non-detections were extracted from the cube in essentially the same way as the spectra with a detected line emission shown in Figs 2 and 3. For the spectra with a detected emission, rms calculations were confined to the emission free part of the spectrum. The 1σ noise levels are listed in Table 3. They vary from spot to spot for the high frequency transitions due to the small primary beam size (comparable with the spread of the spots in the source) and the lack of an adequate mosaicing in the north–south direction. The noise levels list in Table 3 are the uncertainties of the peak flux densities in Table 2 (eighth column).

3.3 Notes on temporal variability

Methanol masers are known to be variable (e.g. Caswell, Vaile & Ellingsen 1995a; Goedhart, Gaylard & van der Walt 2004), although the subject is not very well studied for class I masers. One of the goals of this work is to provide data for further development of maser models. The models are usually checked by comparing the flux density ratios of different transitions. However, these ratios can be affected not only by the studied pumping mechanism, but also by any temporal variability, if observations are not simultaneous. Temporal variability is typically not included in modelling and requires a long time series of data to be well understood. To obtain some estimate of the scale of temporal variability in the source, we repeated the observations of some transitions in different observing runs, in two cases (see Table 1) without a proper imaging (a single short scan). Provided the position of the source is known from another observing run, such non-imaging data still allows us to estimate the

Table 2. Fit results and profile parameters. The uncertainties are given in parentheses and expressed in units of the least significant figure.

Spot	Gaussian components						Peak	Peak		
	LSR velocity[a] ($km\,s^{-1}$)	α_{2000} 16^h58^m (^{s})	δ_{2000} -42° (arcmin arcsec)	Line FWHM ($km\,s^{-1}$)	Flux density (Jy)	Size (arcsec)	LSR velocity[b] ($km\,s^{-1}$)	flux density[c] (Jy)	$\int f(v)\,dv$ ($Jy\,km\,s^{-1}$)	T_b limit (K)
A			5_{-1}–4_0 E (84 GHz)				−32.82	14.6	11.39 (7)	4.5×10^4
	−32.79	16.585 (2)	52 29.56 (2)	0.72 (2)	14.6 (3)	0.40 (6)				
	−31.83	16.516 (8)	52 28.42 (8)	0.25 (9)	0.8 (3)	1.0 (3)				
			8_0–7_1 A^+ (95 GHz)				−32.80	38.80	32.7 (1)	9.5×10^4
	−32.793	16.595 (1)	52 29.74 (1)	0.775 (6)	38.6 (3)	0.3 (2)				
	−31.77	16.527 (9)	52 28.68 (8)	0.28 (4)	2.1 (3)	0.9 (2)				
B			9_{-1}–8_{-2} E (9.9 GHz)				−31.56	9.5	2.80 (4)	5.3×10^7
	−31.572	16.460 (2)	52 25.73 (3)	0.32 (1)	8.1 (3)	0.10 (9)				
	−31.554[d]			<0.029[e]	2.4 (3)					
			2_2–2_1 E (25 GHz)				−31.71	0.3	0.032 (3)	2.8×10^4
	−31.69	16.44 (2)	52 26.4 (2)	0.15 (8)	0.2 (1)	3 (2)				
			3_2–3_1 E (25 GHz)				−31.61	5.9	1.303 (8)	2.6×10^6
	−31.620	16.459 (2)	52 25.90 (4)	0.186 (7)	5.2 (2)	0.08 (3)				
	−31.63[d]			0.46 (16)	0.6 (2)					
			4_2–4_1 E (25 GHz)				−31.71	8.7	2.17 (6)	3.9×10^6
	−31.715	16.459 (2)	52 25.90 (4)	0.203 (7)	8.3 (3)	0.24 (6)				
	−31.8[d]			0.5 (3)	0.6 (3)					
			5_2–5_1 E (25 GHz)				−31.69	6.7	1.80 (2)	3.0×10^6
	−31.678	16.461 (8)	52 25.70 (11)	0.211 (5)	6.4 (2)	0.093 (8)				
	−31.82[d]			0.3 (1)	0.5 (2)					
	−31.24	16.581 (6)	52 25.5 (1)	0.5 (2)	0.4 (2)	0.5 (4)				
			6_2–6_1 E (25 GHz), May				−31.69	7.5	2.047 (4)	3.3×10^6
	−31.701	16.464 (3)	52 25.76 (5)	0.211 (5)	7.3 (2)	0.17 (7)				
	−31.89[d]			0.18 (6)	0.5 (2)					
	−31.23	16.594 (1)	52 25.32 (2)	0.5 (1)	0.6 (2)	0.4 (1)				
			6_2–6_1 E (25 GHz), June				−31.67	7.2	1.88 (6)	6.4×10^6
	−31.649	16.454 (1)	52 25.70 (2)	0.203 (9)	6.8 (3)	0.079 (7)				
	−31.80[d]			0.22 (9)	0.8 (3)					
	−31.2	16.581 (1)	52 25.25 (1)	0.5 (3)	0.5 (3)	0.17 (5)				
			7_2–7_1 E (25 GHz)				−31.64	6.8	1.77 (4)	5.9×10^6
	−31.660	16.462 (1)	52 25.73 (1)	0.24 (1)	6.6 (3)	Unresolved				
	−31.3	16.592 (2)	52 25.26 (3)	0.3 (2)	0.4 (3)	0.28 (5)				
			8_2–8_1 E (25 GHz)				−31.67	5.6	1.48 (2)	4.9×10^6
	−31.644	16.461 (3)	52 25.78 (5)	0.24 (1)	5.5 (3)	0.060 (8)				
			9_2–9_1 E (25 GHz)				−31.63	3.9	0.956 (4)	3.3×10^6
	−31.62	16.458 (1)	52 25.70 (1)	0.24 (2)	3.6 (3)	0.06 (2)				
			5_{-1}–4_0 E (84 GHz)				−31.58	12.3	5.35 (2)	3.7×10^4
	−31.85	16.470 (8)	52 26.29 (6)	0.38 (3)	2.5 (2)	0.8 (4)				
	−31.561	16.454 (2)	52 25.72 (2)	0.215 (5)	9.3 (2)	0.46 (8)				
	−31.31	16.470 (5)	52 25.73 (4)	0.59 (4)	3.4 (2)	0.68 (8)				
			8_0–7_1 A^+ (95 GHz)				−31.52	27.90	19.0 (1)	6.8×10^4
	−32.35	16.469 (2)	52 26.52 (2)	0.59 (6)	2.8 (2)	0.4 (1)				
	−31.808	16.467 (5)	52 26.15 (4)	0.415 (9)	7.2 (2)	0.7 (1)				
	−31.516	16.463 (1)	52 25.83 (1)	0.329 (3)	20.3 (2)	0.30 (2)				
	−31.235	16.473 (3)	52 25.86 (3)	0.594 (9)	10.4 (2)	0.60 (5)				
	−30.56	16.48 (1)	52 26.1 (1)	0.46 (8)	1.0 (2)	1.3 (5)				
			11_{-1}–10_{-2} E (104 GHz)				−31.60	9.59	2.348 (3)	2.0×10^4
	−31.594	16.462 (2)	52 25.64 (2)	<0.022[e]	2.2 (1)	0.2 (1)				
	−31.580[d]			0.293 (5)	7.5 (1)					
C			5_{-1}–4_0 E (84 GHz)				−30.77	2.1	0.7 (1)	6.0×10^3
	−31.14	16.71 (1)	52 20.7 (1)	0.30 (5)	1.2 (2)	1.0 (1)				
	−30.77	16.672 (2)	52 20.62 (2)	0.28 (4)	1.3 (2)	0.4 (2)				
			8_0–7_1 A^+ (95 GHz)				−30.76	7.92	3.549 (3)	1.9×10^4
	−31.46	16.75 (1)	52 20.7 (1)	0.32 (5)	0.7 (1)	2.0 (5)				
	−31.167	16.707 (2)	52 20.85 (1)	0.270 (8)	3.5 (1)	0.36 (5)				
	−30.747	16.686 (2)	52 20.79 (1)	0.276 (4)	7.8 (1)	0.36 (3)				

Table 2 – *continued*

Spot	Gaussian components: LSR velocity[a] ($km\,s^{-1}$)	α_{2000} 16^h58^m (^{s})	δ_{2000} -42° (arcmin arcsec)	Line FWHM ($km\,s^{-1}$)	Flux density (Jy)	Size (arcsec)	Peak LSR velocity[b] ($km\,s^{-1}$)	Peak flux density[c] (Jy)	$\int f(v)\,dv$ ($Jy\,km\,s^{-1}$)	T_b limit (K)
D			(Marginal detection) 5_{-1}–4_0 E (84 GHz)				−30.77	3.0	0.8 (2)	
	−30.8			0.6 (2)	1.5 (5)					
			8_0–7_1 A^+ (95 GHz)				−30.51	9.5	7.54 (4)	1.7×10^4
	−30.92	16.82 (1)	51 59.63 (9)	0.29 (3)	5.3 (5)	0.7 (6)				
	−30.45	16.850 (7)	51 59.98 (5)	0.62 (4)	9.0 (5)	0.7 (3)				
E			(Marginal detection) 5_{-1}–4_0 E (84 GHz)				−30.33	1.5	0.4 (1)	
	−32.18			0.09 (5)	0.5 (3)					
	−30.336			0.05 (1)	1.2 (3)					
	−30.2			0.9 (7)	0.3 (3)					
			8_0–7_1 A^+ (95 GHz)				−30.41	7.1	3.29 (9)	1.6×10^4
	−33.28	17.53 (1)	52 05.14 (9)	0.16 (3)	1.1 (2)	1.0 (5)				
	−31.40	17.72 (1)	52 03.80 (8)	0.12 (4)	0.5 (2)	2 (2)				
	−31.16	17.48 (2)	52 03.9 (2)	0.19 (5)	0.8 (2)	1.4 (3)				
	−30.403	17.549 (4)	52 04.09 (3)	0.210 (8)	5.1 (2)	0.62 (3)				
	−30.185	17.551 (2)	52 04.30 (1)	0.32 (1)	5.2 (2)	0.38 (7)				
F			5_{-1}–4_0 E (84 GHz)				−27.28	20.4	9.3 (2)	5.8×10^4
	−27.87	16.2 (1)	52 00 (1)	0.18 (5)	1.7 (4)	Unresolved				
	−27.436	16.163 (7)	52 01.02 (6)	0.37 (1)	11.1 (4)	0.8 (3)				
	−27.311	16.187 (8)	52 00.99 (6)	0.106 (5)	9.8 (4)	0.8 (2)				
	−27.108	16.146 (5)	52 00.73 (4)	0.254 (9)	12.8 (4)	0.6 (3)				
			8_0–7_1 A^+ (95 GHz)				−27.14	36.6	20.56 (7)	8.7×10^4
	−27.94	16.190 (7)	52 01.14 (6)	0.10 (2)	2.0 (3)	0.9 (4)				
	−27.75	16.149 (4)	52 01.11 (3)	0.16 (2)	3.5 (3)	0.5 (2)				
	−27.321	16.171 (3)	52 01.23 (2)	0.482 (5)	30.3 (3)	0.53 (5)				
	−27.094	16.156 (1)	52 01.13 (1)	0.238 (5)	16.9 (3)	0.36 (4)				

[a]The uncertainty is half of that for the line FWHM.
[b]The uncertainty is the spectral resolution listed in Table 1.
[c]The uncertainty is the rms listed in Table 3.
[d]The position is the same as for the component above as they cannot be distinguished in the image.
[e]The given upper limit is the spectral resolution rather than a FWHM estimate.

Table 3. The noise level (1σ rms) in the spectra.

Transition and frequency	Maser spot: A	B	C	D	E	F
	1σ rms (Jy)					
9_{-1}–8_{-2} E (9.9 GHz)	0.3 for all spots					
J_2–J_1 E (May) (25 GHz)	0.1 for all spots					
J_2–J_1 E (June) (25 GHz)	0.2 for all spots					
5_{-1}–4_0 E (84 GHz)	0.2	0.2	0.2	0.5	0.3	0.5
8_0–7_1 A^+ (95 GHz)	0.09	0.09	0.07	0.3	0.2	0.4
11_{-1}–10_{-2} E (104 GHz)	0.1	0.07	0.08	0.4	0.3	0.5

peak flux density and, therefore, to assess the variability. We have performed calibration similar to that used for the main data set and obtained the following estimates for the peak flux density by fitting a point source at the known position to the visibility data: 6.7 ± 0.2 Jy for the 25-GHz $J = 6$ data taken in the August session, and 9.0 ± 0.2 Jy for the 9.9-GHz data taken in May. The 25-GHz $J = 6$ transition was observed in all three sessions, and the above value of the flux density is in agreement with that in Table 2 within 3σ uncertainty. The 9.9-GHz non-imaging data are in agreement with the corresponding imaging experiment as well. The latter is also important for our conclusion that polarization effects do not significantly affect the results of our observations (Section 2). This is because, in contrast to the June observations, the 9.9-GHz non-imaging observations carried out in May used a dual polarization mode and provided effectively a Stokes I measurement. Taking into account the systematic errors in establishing the absolute flux density scale, which are estimated to be around 10 and 3 per cent at 25 and 9.9 GHz, respectively, we can conclude any temporal variability within the period of our observations is less than the calibration errors. Therefore, we can consider that we have inputs for the modelling which are free from any significant variability bias.

4 DISCUSSION

4.1 Association with outflow

All the detected maser spots are located within a dense molecular core (deconvolved FWHM 27 arcsec; Garay et al. 2003) and have velocities close to that of the ambient molecular material in the core ($-30.0\,km\,s^{-1}$). A remarkable correlation between the southern maser spots (labelled A to C) and the shocked gas mentioned in Section 3.1 (see also Fig. 1) points to an association of the class I masers with the interface region of this outflow. This result is somewhat similar to that obtained for the northern star-forming region DR 21 by Plambeck & Menten (1990) more than a decade ago. In addition, Kurtz et al. (2004) revealed the same association for a few other northern sources. However, a more favourable geometry and probably lesser complexity in the IRAS 16 457−4247 star-forming region allows us to study this association in detail.

In contrast to the southern spots, no associated H_2 emission has been detected in the vicinity of the northern spots E and F (see Fig. 1). However, spot D resides close to the northern continuum lobe, which is associated with faint H_2 emission. This morphology leaves no doubts that spot D is very similar to the southern maser spots, because the continuum source represents a working surface of the jet (Brooks et al. 2003). Moreover, it is evident from the large-scale image of the H_2 emission (Fig. 1) that an outflow lobe extending northwards is present. Therefore, it is likely that all maser spots in this source are associated somehow with the molecular outflow. Two factors or their combination can explain the non-detection of the H_2 emission in the vicinity of the maser spots E and F. First, the 2.12-μm H_2 emission can be affected by extinction, which may be higher in the northern part of the region. Such variations of extinction have been observed in other sources (e.g. Eislöffel, Smith & Davis 2000; Nanda Kumar, Bachiller & Davis 2002). In addition, Garay et al. (2006) have recently discovered a bipolar molecular outflow towards IRAS 16 457−4247. This outflow is inclined to the line of sight at an angle of 40° with the receding flow located in the northern part of the region. A higher extinction to the north from the central object has a natural explanation in this geometry.

Alternatively, or in addition to this, the conditions in the interface region may be less energetic in the northern part of the source, if for example most of the dense material blocking the path of the outflow has already been swept away. The cooling time-scale of the gas radiating shocked H_2 emission is very short and may be of the order of several years (e.g. Smith & Brand 1990; Davis & Smith 1995). This estimate is in agreement with measurements of variability performed by Micono et al. (1998) for the HH 46/47 outflow system. Because the IRAS 16 457−4247 outflow extends well beyond the region containing maser spots (see Fig. 1), the shocked gas in the vicinity of northern maser spots generated when the jet carved out a cavity in the dense molecular core has already had enough time to radiate the energy and cool down if the interaction became less energetic for some reason. It is reasonable to expect that the shocks associated with internal working surfaces (where a fast moving gas impacts a slow moving gas and drives shocks into the medium) are less energetic than those associated with the terminal working surfaces (where the flow impacts the cloud directly). To the south from the central source, the jet may have impacted the walls of the cavity generating a young curved shock. However, as it was mentioned above, there are a number of other factors that can account for the shape of this H_2 feature. It must be noted that this scenario is speculative as there is no direct observational evidence at this stage that suggests a weaker interaction of the northern flow with the cloud.

The main role of shocks for methanol maser formation is thought to be that they increase the methanol abundance in the gas phase. The production of methanol by purely gas-phase chemical reactions is inefficient, but the passage of weak shocks is able to release it from the grain mantles (e.g. Hartquist et al. 1995). Shocks generated due to the interaction between outflows and the ambient material are known to enhance the methanol abundance (e.g. Gibb & Davis 1998; Garay et al. 2002). In addition, outflows compress the medium, which makes collisions more frequent and the pumping mechanism more efficient. The shocks have to be relatively gentle as methanol can survive sputtering or desorption of grain mantles only at shock velocities not greatly exceeding 10 km s^{-1} (Garay et al. 2002). Therefore, class I methanol masers are likely to reside in the wakes associated with the bow shocks or internal working surfaces rather than near the apex of a terminal bow shock. The fact that all maser spots are only found close to the jet (Fig. 1) supports this idea.

It is worth noting that spot B, which is active in all observed transitions, is located near the edge of the brightest H_2 knot. It is the only spot in this source where maser emission at 9.9, 25 and 104 GHz has been detected. According to models calculated by Sobolev et al. (2005) these masers require more energetic conditions (higher densities and temperatures) than the common masers at 84 or 95 GHz. Our results confirm this model, although with the caveat that the observed H_2 emission may be affected by variable extinction. Spectroscopy of a number of H_2 transitions, as well as observations of other shock tracers less prone to extinction (e.g. SiO and thermal methanol transitions) are required before firm conclusions can be drawn. The 9.9- and 104-GHz profiles contain a narrow spike (Fig. 3) which has a width comparable to the spectral resolution (<0.03 km s^{-1}, see Table 1), and is the narrowest spectral feature ever claimed according to our knowledge. Such a narrow feature implies that the maser is unsaturated and requires turbulent motions to be suppressed (e.g. by the magnetic field) in the gas involved in the maser action.

The clear association of class I methanol masers with outflows in this and other sources suggests that searches for class I methanol masers should be extended to sites of intermediate- and low-mass star formation, where outflows are common (Reipurth & Bally 2001). Indeed, at such sites a few class I masers have recently been found (Kalenskii et al. 2006), but a lack of accurate positions for these masers means their association with outflows cannot be verified at the present.

4.2 Masers at 84 and 95 GHz

As mentioned above, the maser profiles at 84 and 95 GHz look similar in general (Figs 2 and 3). This suggests a common range of physical conditions required for these masers to form. Val'tts et al. (2000) found a similar correspondence between the 95-GHz masers and the 7_0–6_1 A^+ masers at 44 GHz (this frequency is currently outside the band of the ATCA receivers and has not been observed in this project) using a large sample of southern maser sources, including IRAS 16 547−4247. The flux densities of these two transitions were found to correlate, despite a significant scatter of the points, which is most likely caused by the lack of accurate positions for the majority of known class I methanol masers. However, the 44- and 95-GHz masers belong to the same $(J+1)_0$–J_1 A^+ series of transitions ($J = 6$ and 7, respectively) and are expected to correlate. In contrast, the 84 and 95-GHz maser transitions belong to a different series of transitions, and even to different species of methanol (E- and A-methanol, respectively, see Table 1), which act as two different molecules. Therefore, a correlation between the flux densities corresponding to these two transitions is not self-evident and can be a constraining factor for models of maser pumping.

Fig. 4 shows the peak flux densities (F) at 84 and 95 GHz for matching pairs of the Gaussian components listed in Table 2. Each point is labelled with the spot name and the peak velocities of the corresponding 84- and 95-GHz Gaussian components. The error bars show 3σ formal uncertainties of the fit and do not take into account possible systematic errors due to the absolute flux density scale and the structure of each spectral profile. It was concluded from the general appearance of the profiles that the spot F is likely to have an additional component at 95 GHz. Therefore, the systematic errors are particularly acute for this spot. Despite this caveat, Fig. 4 reveals the correlation between flux densities quite well. A linear least-square fit gives the following dependence:

$$\mathrm{F(95\,GHz)} = (2.1 \pm 0.3)\mathrm{F(84\,GHz)} + (2.6 \pm 2.5), \quad (1)$$

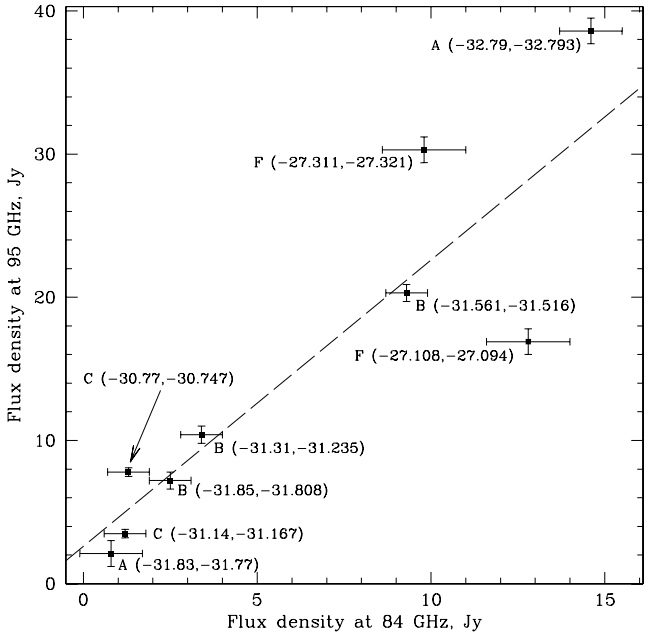

Figure 4. The correlation between flux densities at 84 and 95 GHz. Each data point is labelled with the spot name and velocities in km s^{-1} (two numbers in brackets) corresponding to the 84- and 95-GHz components taken from Table 2. The error bars correspond to the 3σ formal uncertainty of the Gaussian fit. The dashed line with the slope 2.1 ± 0.3 represents the least-square fit discussed in the text.

which is shown in Fig. 4 by the dashed line. The additive term is not statistically significant. The absolute flux density scale calibration affects all spots at the same frequency in the same way. Therefore, the slope has an additional uncertainty of 30 per cent (about 0.6). Kalenskii et al. (2001) obtained a similar result to (1) by comparing single dish surveys of a large number of sources at these two frequencies. However, to study such a dependence reliably, an interferometer is required, due to the spread of maser spots. It is worth mentioning that interferometric observations of the DR 21 star-forming complex carried out by Batrla & Menten (1988) and Plambeck & Menten (1990), found the ratio of the 95- to 84-GHz flux density to be approximately 5.5, somewhat higher than observed in IRAS 16 547−4247.

4.3 Rest frequencies

High spectral resolution observations can be used to improve the accuracy to which the transition rest frequencies are known. However, in many cases, the laboratory measurement is preferred regardless of its accuracy because the assumption of equal velocities for all transitions may be misleading (e.g. the discussion about the 95- and 25-GHz masers in the next section). According to Fig. 3 the 9.9- and 104-GHz transitions have a single channel spike on top of the broad line. These two transitions belong to the same $(J+1)_{-1}$–J_{-2} E transition series ($J = 8$ and 10) and are expected to show a similar behaviour. Therefore, assuming that the spike is at the same velocity, the rest frequency of the 9_{-1}–8_{-2} E transition is 9936.201 ± 0.001 MHz. The uncertainty is determined by the spectral resolution at 9.9 and 104 GHz and the rest frequency uncertainty of the 104-GHz transition. The rest frequency was adjusted with respect to Table 1 by 1 kHz or 0.03 km s^{-1}. It is not practical to adjust the rest frequency for other transitions.

4.4 Maser models

Theoretical studies of class I methanol masers were impeded for a long time by the absence of an adequate model of collisions for the methanol molecule. Recently calculated rate coefficients (e.g. Pottage, Flower & Davis 2004) have encouraged pumping studies of these masers. Sobolev et al. (2005) performed a qualitative analysis and revealed that the 25-GHz masers are bright in models with specific column density (equivalent to the column density divided by the linewidth) greater than 10^{12} cm^{-3} s and require relatively high kinetic temperatures (75–100 K) and densities (10^5–10^7 cm^{-3}). Similar conditions are required for the 9.9- and 104-GHz masers, although they prefer a greater beaming (elongated geometry) and either lower densities or higher temperatures (more than 100 K). Spot B is an excellent test site to develop a class I pumping model because of the large number of transitions detected. However, a detailed investigation of the vast parameter space of the maser models is beyond the scope of this paper and will be reported elsewhere. At present we are unable to reproduce the relative brightnesses of all transitions detected in spot B in a single model similar to that of Sobolev et al. (2005). We suspect that gradients in the physical parameters may be influential and leading to the co-existence of the different pumping regimes on spatial scales unresolved by ATCA. It is expected that strong gradients may accompany shocks, although their effects on the maser pumping are yet to be studied. According to Table 2 the peak components at 25 and 95 GHz are displaced by not more than 0.1 arcsec. Most likely this displacement is caused by a systematic error due to the structure of the 95-GHz maser because no such displacement is observed for the 84-GHz maser. Taking this uncertainty as an upper limit and assuming a distance to the source of 2.9 kpc, the parameters must change on a scale around 300 au or less.

It is worth noting, however, that firm conclusions about any gradients can only be made after an extensive parameter search. In this paper we have just illustrated the situation using two representative models selected from the range of models calculated by Sobolev et al. (2005). Outlines of the modelling procedure applicable to class I masers can be found in Voronkov et al. (2005b) and the code is described by Sutton et al. (2004) and references therein. Both models use a kinetic temperature ($T_{\rm gas}$) of 75 K, an intrinsic linewidth (to simulate blending of spectral lines) of 0.5 km s^{-1}, and a methanol abundance relative to hydrogen of 10^{-5}. The parameters that differ between these two models are the hydrogen number density ($n_{\rm H}$), 10^7 and 10^6 cm^{-3}, the specific column density (equivalent to the column density divided by the linewidth), 10^{12} and $10^{10.5}$ cm^{-3} s, and the beaming factor (ε^{-1}), 20 and 30, for the first and the second models, respectively. The results of the simulations are shown in Table 4. Most of the columns are self-explanatory, the columns labelled $\log R$ give a decimal logarithm of the ratio of the integrated flux density of the transition to that of the $J = 4$ 25-GHz transition (as observed and for each of the models). The uncertainties of the observed $\log(R)$ are given in the parentheses and expressed in units of the least significant figure. These are cumulative uncertainties, which, in general, account for both the absolute flux density scale uncertainty and that of the integrated flux density given in Table 2. The $J = 2$ and 3 transitions were observed simultaneously with the reference ($J = 4$) transition in the same band (see Section 2). Therefore, the ratio R is not affected by the absolute flux density scale calibration for these two transitions. Other columns contain the brightness temperatures ($\log T_{\rm b}$) and optical depths (τ) predicted by the two models.

Fig. 5 illustrates the dependence of $\log R$ on the excitation energy for the 25-GHz series (data from Table 4). Open squares and

Table 4. Model results for spot B. R is the ratio of the integrated flux density to that of the $J = 4$ transition at 25 GHz, τ is the optical depth and T_b is the brightness temperature. The uncertainties of the observed log (R) are given in the parentheses and expressed in units of the least significant figure. According to Table 2 the brightness temperature of the $J = 4$ 25-GHz transition exceeds 3.9×10^6 K.

Transition		ν	Observed	Model 1			Model 2		
		(GHz)	log (R)	log(T_b, K)	τ	log (R)	log ($T_{b,K}$)	τ	log (R)
9_{-1}–8_{-2}	E	9.9	0.11 (7)	8.92	−17.9	−0.1	8.81	−19.1	0.5
2_2–2_1	E	25	−1.8 (1)	6.34	−10.1	−1.9	5.29	−9.9	−2.2
3_2–3_1	E	25	−0.22 (4)	7.98	−13.7	−0.3	7.36	−14.6	−0.2
4_2–4_1	E	25	0						
5_2–5_1	E	25	−0.08 (8)	8.34	−14.3	0.1	7.55	−14.9	0
6_2–6_1	E (May)	25	−0.03 (7)	8.43	−14.5	0.2	7.36	−14.5	−0.2
6_2–6_1	E (June)	25	−0.1 (1)						
7_2–7_1	E	25	−0.09 (9)	8.47	−14.7	0.2	7.00	−13.7	−0.5
8_2–8_1	E	25	−0.17 (8)	8.45	−14.7	0.2	6.27	−12.2	−1.3
9_2–9_1	E	25	−0.36 (7)	8.45	−14.8	0.2	5.36	−10.2	−2.2
5_{-1}–4_0	E	84	0.4 (1)	2.38	20.9	−4.8	6.95	−12.3	0.5
8_0–7_1	A^+	95	0.9 (1)	1.95	71.9	−5.1	6.83	−11.9	0.4
11_{-1}–10_{-2}	E	104	0.0 (1)	2.93	1.2	−4.1	5.58	−10.7	−0.7

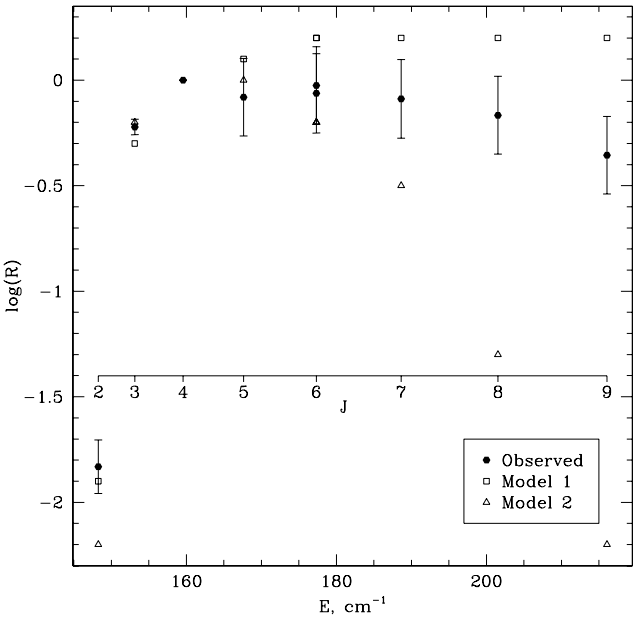

Figure 5. The dependence of the observed and predicted relative integrated flux densities (R) versus the excitation energy for the 25-GHz masers detected in spot B. Open squares and triangles correspond to the first and the second models (see Table 4), respectively. Observed values are represented by the filled circles. The $J = 4$ transition is taken as a reference (see text). Therefore, the observed point and the model points coincide exactly for this transition. The error bars for observed values represent a cumulative 3σ uncertainty, which takes into account the uncertainty of the absolute flux density scale for $J > 4$ transitions ($J = 2$, 3 and 4 transitions were observed simultaneously in the same band; see Section 2). There are two independent observations of the $J = 6$ transition.

triangles correspond to the first and the second models, respectively. Observed values are shown by the filled circles with error bars corresponding to the 3σ uncertainty. The observed dependence represents essentially a rotational diagram (because the product of the spontaneous decay rate by the statistical weight does not vary much throughout the series), which is a well-known method to analyse the level populations of the molecule (e.g. Menten et al. 1986). The plot of observed values shows a significant curvature, although a linear fit to the highest J transitions is possible. Such a fit, which takes into account all transitions with $J > 3$, has a rotational temperature of 80 ± 10 K. It should be remembered that this temperature is unlikely to be related to any physical or even excitation temperature. The latter is estimated correctly if the fitted 25-GHz transitions are all optically thin or have the same optical depth.

It is evident from Table 4 that despite the fact that the first model describes the ratios for the 9.9 and the 25-GHz transitions quite well, it fails to produce the masers at 84, 95 and 104 GHz. Similarly, the second model is adequate for 9.9-, 84-, 95- and 104-GHz masers, but fails to describe the behaviour of the high J 25-GHz transitions (Fig. 5). The brightness temperature of the reference 4_2–4_1 E transition is 1.9×10^8 and 3.6×10^7 K for the first and the second models, respectively (see Table 4). Both these values are in agreement with the observed lower limit (3.9×10^6 K, Table 2).

4.5 Evolutionary stages and maser activity

H_2O, OH and both classes of methanol masers often, but not always, are present in the same region of high-mass star formation. The question whether these masers trace an evolutionary sequence (with a partial overlap in time) has been investigated in various studies (e.g. Forster & Caswell 1989; Codella & Moscadelli 2000; Ellingsen 2005, 2006; Szymczak, Pillai & Menten 2005). From their analysis of a large sample of star-forming regions Forster & Caswell (1989) concluded that the compact, isolated H_2O masers mark the earliest evolutionary stages, and OH masers appear afterwards. The class II methanol masers at 6.7 GHz seem to largely overlap with the H_2O masers and precede OH (e.g. Szymczak et al. 2005). The majority of class II masers are not associated with detectable HII regions (Phillips et al. 1998; Walsh et al. 1998), but show an association with millimetre and submillimetre (Pestalozzi, Humphreys & Booth 2002; Walsh et al. 2003) sources which leaves no doubt that they trace a very early stage of the (proto)stellar evolution. However, the question as to where the class I methanol masers fit into this picture is still poorly understood. The main obstacle is the lack of untargeted surveys of class I masers, which have not been undertaken mainly because there is no widespread, bright, low-frequency maser transition similar to the 6.7 GHz class II transition or main-line OH. Most class I masers, except for a few famous sources like OMC-1, have been found towards known class II methanol or

OH maser sites, which are often located within a single dish beam (e.g. Slysh et al. 1994; Ellingsen 2005). Therefore, all these samples are biased. Ellingsen (2006) investigated this question using the infrared properties of a subsample of methanol masers associated with GLIMPSE (Galactic Legacy Infrared Mid-Plane Survey Extraordinaire) catalogue point sources. Despite the small number statistics, which makes any firm conclusions impossible, it was found that the sources with a class I maser seem to have redder GLIMPSE colours than those without it. Based on these results, Ellingsen (2006) concluded that the class I methanol masers may signpost an earlier stage of high-mass star formation than the class II masers.

Forster & Caswell (1989) detected both mainline OH and H_2O masers in IRAS 16 547−4247 at a position close to the central continuum source in Fig. 1. Taking into account the information given in the previous paragraph, one may expect the source to be relatively old and most likely to be active in class II maser transitions. It is generally assumed that each high-mass star-forming region has a detectable 6.7-GHz maser sometime during the early stages of its evolution regardless of the maser variability and the source geometry (e.g. van der Walt 2005). However, no 6.7-GHz emission has been detected in this source (upper limit of 0.3 Jy; Caswell et al. 1995b; Walsh et al. 1998), in contrast to the detection of the large number of class I masers reported in this paper. This fact encourages us to revisit the question of where class I methanol masers fit into an evolutionary sequence.

The GLIMPSE survey (Benjamin et al. 2003) provides mid-infrared (MIR) images of the Galactic plane with unprecedented sensitivity. Fig. 6 shows the locations of the radio continuum, methanol, OH and water masers superimposed on the GLIMPSE 5.8-μm emission (grey-scale) on the same scale as Fig. 1. The most striking feature of this image is that there are no MIR sources associated with either the jet source, or the class I masers. Diffuse emission, probably arising from the polycyclic aromatic hydrocarbons (PAH) band at 6.2 μm appears to be associated with the outflow region and traces a similar area to the shock-excited H_2. Although, unlike the H_2, the PAH emission is stronger closer to the central continuum source and very faint in the vicinity of spot B. The GLIMPSE 3.6-μm image shows similar diffuse emission, also likely to be associated with PAH emission, in this case from the 3.3-μm band. Fig. 6 also shows a strong, extended MIR source lying between spots D and F. We have also examined the Midcourse Space Experiment (MSX) images of this region which show that although the 12-μm emission (C band) is centred on the strong MIR source seen in Fig. 6, the 21-μm emission (E band) is offset and centred on the central continuum source. That the source driving the jet/outflow/masers is only visible at wavelengths longer than 12 μm suggests that this source is at a very early evolutionary phase. Garay et al. (2003) argued that the observed cm-wavelength continuum emission towards IRAS 16 547−4247 is too weak for such a luminous object ($6.2 \times 10^4\,L_\odot$). Supported by the characteristics of the spectral line profiles, Garay et al. (2003) explained this flux discrepancy by the ongoing intense accretion, which forbids the development of an ultracompact HII region. Intense accretion is further evidence for an early evolutionary phase. Ellingsen (2006) found the vast majority of class II methanol maser sources to be associated with MIR emission visible in the GLIMPSE 8.0-μm observations. That such emission is absent in this source argues that it is likely to be at an earlier evolutionary phase than that which produces class II methanol masers; however, this is in direct contrast with the presence of OH masers which would generally be taken to support the opposite interpretation.

In theory, a moderately dense gas (dense enough to switch the collisional pumping on, but not dense enough to produce

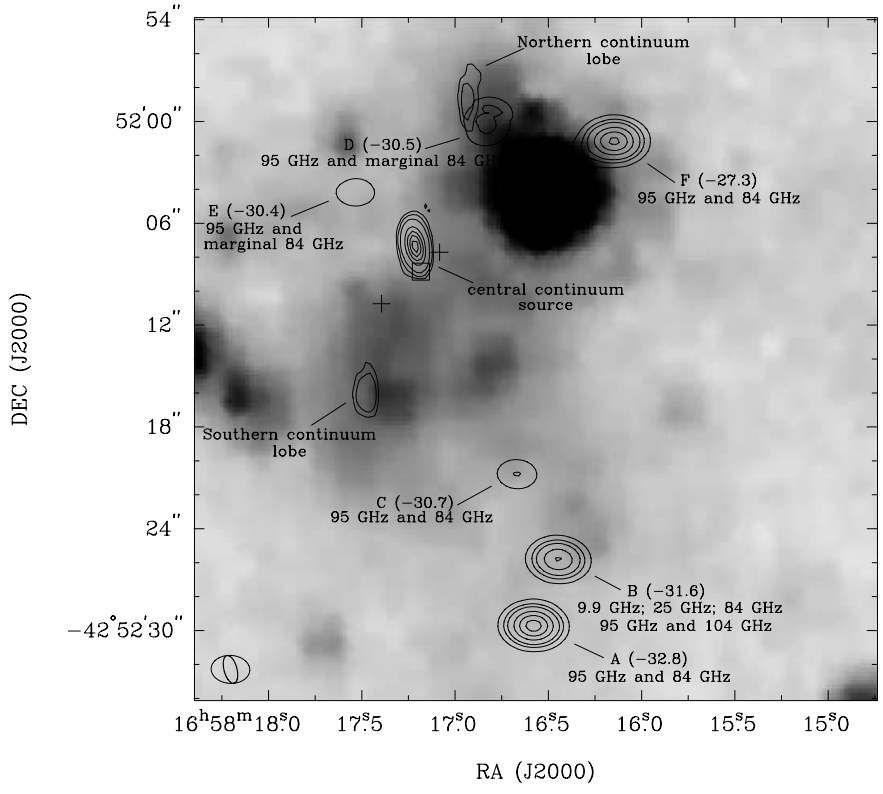

Figure 6. The same as the inset in Fig. 1, but with the GLIMPSE 5.8-μm emission shown by grey-scale.

thermalization), rich in methanol and separated from strong infrared sources is able to produce most class I methanol masers (Cragg et al. 1992; Voronkov 1999; Voronkov et al. 2005b). The fact that the class I masers do not require infrared radiation for pumping suggests that they might exist at earlier evolutionary stages than the class II masers, which need a nearby infrared source for pumping. However, a mechanism able to increase the methanol abundance above that seen in cold cores must already be active or have been active in the past to produce a detectable maser. As was discussed above, a release of methanol from the grain mantles by weak shocks is a good example of such a mechanism. One cannot exclude the possibility that class I masers survive even when the shock, which had increased the methanol abundance in the past, has already dissipated. Rare class I masers at 9.9 and 104 GHz require more energetic conditions (Sobolev et al. 2005). They are most likely (or even exclusively) located near the young shocks. Spot B in Fig. 1 is likely to be a good example of such a situation. If the idea that the common class I masers can outlast the shock is correct, these masers become hard to destroy, once they appear. Situated at a considerable distance from the central object they probably fade out slowly as the methanol abundance decreases (e.g. due to freeze out or gas-phase chemical processing; Avery & Chiao 1996), unless the chemical composition of the medium is altered once again by new energetic outflow events or by a slight change in the outflow direction. A new epoch of interaction between the outflow and the medium can either destroy the molecules engaged in the maser emission or produce new masers. Assuming typical outflow velocities of 10^2–10^3 km s^{-1}(e.g. Reipurth & Bally 2001), it would take at least 10^4–10^5 yr for this disturbance to reach the maser sites for the given distance to the source (2.9 kpc) and the angular separations of masers from the central object (see Table 2). A time-scale for methanol destruction by ion–molecule reactions has approximately the same order of magnitude (e.g. Sandford & Allamandola 1993; Garay et al. 2002).

The class II masers are usually located very close to the YSO and, therefore, can be more easily destroyed during the course of its evolution. Given the detection of OH masers, which suggests an evolved stage, it is, therefore, possible that the 6.7-GHz maser has already been quenched in the studied source. We cannot presently resolve the contradiction between the infrared data and the presence of OH masers and confidently determine whether the source is too young or too old to have a 6.7-GHz maser. However, these speculations show that the evolutionary stage where the class I masers are active, may in fact last longer and start earlier than when the class II masers are active.

5 CONCLUSIONS

(i) The class I methanol maser emission consists of a cluster of six spots spread over an area of 30 arcsec in extent. Five spots were detected in only the 84- and 95-GHz transitions (for two spots the 84-GHz detection is marginal), while the sixth spot shows activity in all 12 observed transitions.

(ii) The three most southern maser spots show clear association with a jet-driven molecular outflow. Their velocities are close to that of the molecular core within which the jet is embedded. This fact supports the idea that the class I masers reside in the interface regions of outflows.

(iii) Comparison with OH masers and infrared data reveals a potential discrepancy in the expected evolutionary state: the presence of the OH masers usually means that the source is evolved, but the infrared data suggest otherwise. The class II methanol masers at 6.7 GHz are very widespread and are usually treated as an inevitable phenomenon at some stage of high-mass protostellar evolution (see Section 4.5). The lack of such a maser in this source (which is active in many class I maser transitions) raises an additional question concerning its evolutionary state: whether this source is too young or too old to have a 6.7-GHz maser? We argue that both cases are possible because the class I masers do not require an infrared source for pumping and are harder to destroy than the class II masers, which are usually located close to the YSO. We, therefore, suggest that the evolutionary stage where the class I masers are present may last longer than that with the class II masers, although the exact status of this source is not clear at present.

(iv) We report the first interferometric observations of the rare 9.9- and 104-GHz masers. The spectra for these transitions contain a very narrow spike ($<$0.03 km s^{-1}) which has a brightness temperature greater than 5.3×10^7 and 2.0×10^4 K at 9.9 and 104 GHz, respectively.

(v) High spectral resolution data leads us to suggest that the rest frequency for the 9_{-1}–8_{-2} E transition should be refined to 9936.201 ± 0.001.

ACKNOWLEDGMENTS

We would like to thank Prof. Brian Boyle, the director of the Australia Telescope, for granting an additional observing time for the project on June 16. We also appreciate the efforts of an anonymous referee, whose suggestions helped to improve the quality of this publication. The Australia Telescope is funded by the Commonwealth of Australia for operation as a National Facility managed by CSIRO. SPE thanks the Australian Research Council for financial support for this work. This research has made use of NASA's Astrophysics Data System Abstract Service. This research has made use of data products from the MSX. Processing of the MSX data was funded by the Ballistic Missile Defence Organization with additional support from the NASA Office of Space Science. This research has made use of data products from the GLIMPSE survey, which is a legacy science program of the Spitzer Space Telescope, funded by the NASA. The research has made use of the NASA/IPAC Infrared Science Archive, which is operated by the Jet Propulsion Laboratory, California Institute of Technology, under contract with the NASA.

REFERENCES

Avery L. W., Chiao M., 1996, ApJ, 463, 642
Batrla W., Menten K. M., 1988, ApJ, 329, L117
Benjamin R. A. et al., 2003, PASP, 115, 953
Brooks K. J., Garay G., Mardones D., Bronfman L., 2003, ApJ, 594, L131
Brooks K. J., Garay G., Voronkov M. A., Rodríguez L. F. 2006, ApJ, submitted
Caswell J. L., Vaile R. A., Ellingsen S. P., 1995a, Publ. Astron. Soc. Aust., 12, 37
Caswell J. L., Vaile R. A., Ellingsen S. P., Whiteoak J. B., Norris R. P., 1995b, MNRAS, 272, 96
Codella C., Moscadelli L., 2000, A&A, 362, 723
Cragg D. M., Johns K. P., Godfrey P. D., Brown R. D., 1992, MNRAS, 259, 203
Davis C. J., Smith M. D., 1995, ApJ, 443, L41
Eislöffel J., Smith M. D., Davis C. J., Ray T. P., 1996, AJ, 112, 2086
Eislöffel J., Smith M. D., Davis C. J., 2000, A&A, 359, 1147
Ellingsen S. P., 2005, MNRAS, 359, 1498
Ellingsen S. P., 2006, ApJ, 638, 241
Forster J. R., Caswell J. L., 1989, A&A, 213, 339

Garay G., Mardones D., Rodríguez L. F., Caselli P., Bourke T. L., 2002, ApJ, 567, 980
Garay G., Brooks K. J., Mardones D., Norris R. P., 2003, ApJ, 587, 739
Garay G. et al. 2006, A&A, submitted
Gibb A. G., Davis C. J., 1998, MNRAS, 298, 644
Goedhart S., Gaylard M. J., van der Walt D. J., 2004, MNRAS, 355, 553
Habart E., Walmsley M., Verstraete L., Cazaux S., Maiolino R., Cox P., Boulanger F., Pineau Des Forêts G., 2005, Space Sci. Rev., 119, 71
Hartquist T. W., Menten K. M., Lepp S., Dalgarno A., 1995, MNRAS, 272, 184
Henriksen R. N., Ptuskin V. S., Mirabel I. F., 1991, A&A, 248, 221
Kalenskii S. V., Slysh V. I., Val'tts I. E., Winnberg A., Johansson L. E., 2001, Astron. Rep., 45, 26
Kalenskii S. V., Promyslov V. G., Slysh V. I., Bergman P., Winnberg A., 2006, Astron. Rep., 50, 289
Kurtz S., Hofner P., Álvarez C. V., 2004, ApJS, 155, 149
Mehringer D. M., Menten K. M., 1996, ApJ, 474, 346
Menten K. M., 1996, in van Dishoeck E. F., ed., Proc. IAU Symp. 178, Molecules in Astrophysics: Probes and Processes. Kluwer, Dordrecht, p. 163
Menten K. M., Walmsley C. M., Henkel C., Wilson T. L., 1986, A&A, 157, 318
Micono M., Davis C. J., Ray T. P., Eislöffel J., Shetrone M. D., 1998, ApJ, 494, L227
Müller H. S. P., Menten K. M., Mäder H., 2004, A&A, 428, 1019
Nanda Kumar M. S., Bachiller R., Davis C. J., 2002, ApJ, 576, 313
Pestalozzi M. R., Humphreys E. M. L., Booth R. S., 2002, A&A, 384, L15
Phillips C. J., Norris R. P., Ellingsen S. P., McCulloch P. M., 1998, MNRAS, 300, 1131
Plambeck R. L., Menten K. M., 1990, ApJ, 364, 555
Pottage J. T., Flower D. R., Davis S. L., 2004, J. Phys. B, 37, 165
Reipurth B., Bally J., 2001, ARA&A, 39, 403
Rodríguez L. F., Garay G., Brooks K. J., Mardones D., 2005, ApJ, 626, 953
Salii S. V., Sobolev A. M., Kalinina N. D., 2002, Astron. Rep., 46, 955
Sandford S. A., Allamandola L. J., 1993, ApJ, 417, 815
Slysh V. I., Kalenskii S. V., Val'tts I. E., Otrupcek R., 1994, MNRAS, 268, 464
Smith M. D., Brand P. W. J. L., 1990, MNRAS, 245, 108
Sobolev A. M., 1992, SvA, 36, 590
Sobolev A. M., Ostrovskii A. B., Kirsanova M. S., Shelemei O. V., Voronkov M. A., Malyshev A. V., 2005, in Cesaroni R., Churchwell E. B., Felli M., Walmsley C. M., eds, Proc. IAU Symp. 227, Massiue Star Birth: A Crossroads of Astrophysics. Cambridge Univ. Press, Cambridge, p. 174
Sutton E. C., Sobolev A. M., Salii S. V., Malyshev A. V., Ostrovskii A. B., Zinchenko I. I., 2004, ApJ, 609, 231
Szymczak M., Pillai T., Menten K. M., 2005, A&A, 434, 613
Val'tts I. E., Ellingsen S. P., Slysh V. I., Kalenskii S. V., Otrupcek R., Larionov G. M., 2000, MNRAS, 317, 315
van der Walt D. J., 2005, MNRAS, 360, 153
Voronkov M. A., 1999, Astron. Lett., 25, 149
Voronkov M. A., Sobolev A. M., Ellingsen S. P., Ostrovskii A. B., Alakoz A. V., 2005a, Ap&SS, 295, 217
Voronkov M. A., Sobolev A. M., Ellingsen S. P., Ostrovskii A. B., 2005b, MNRAS, 362, 995
Walsh A. J., Burton M. G., Hyland A. R., Robinson G., 1998, MNRAS, 301, 640
Walsh A. J., Lee J.-K., Burton M. G., 2002, MNRAS, 329, 475
Walsh A. J., Macdonald G. H., Alvey N. D. S., Burton M. G., Lee J.-K., 2003, A&A, 410, 597
Wiesemeyer H., Thum C., Walmsley C. M., 2004, A&A, 428, 479

This paper has been typeset from a TEX/LATEX file prepared by the author.